Journal of Hazardous Materials

Fabrication of Z-scheme Bi7O9I3/g-C3N4 heterojunction modified by carbon quantum dots for synchronous photocatalytic removal of Cr (VI) and organic pollutants
### --Manuscript Draft--

Corresponding Author:	Dekui Shen CHINA
First Author:	Lingli Zhu
Order of Authors:	Lingli Zhu
	Dekui Shen
	Huiyan Zhang
	Kai Hong Luo
	Chong Li

Abstract:	Cr(VI), a highly toxic metal ion, generally co-exists with organic pollutants in industrial effluents. The clean and effective technology for water purification is an imperative issue but still a challenging task. The BOI/CN composite modified by lignin-derived CQD was fabricated by hydrothermal method and applied for synchronous photocatalytic removal of Cr (VI) and levofloxacin (LEV). Compared to those of BOI (51.2%), CN (36.8%) and BOI/CN (74.4%), the photoreduction efficiency of Cr(VI) reached up to 100% by 0.5-CQD/BOI/CN photocatalyst (0.5% content of CQD) under 60 min of light irradiation, together with 94.8% degradation efficiency of LEV. The redox potential in the Z-scheme CQD/BOI/CN system was estimated based on the band structure analysis, revealing that CQD as an electron reservoir constructed a bridge for promoting the electron transfer in BOI/CN heterojunction. The degradation of LEV was dominantly controlled by holes and $\cdot O_2^-$ identified by electron paramagnetic resonance analysis and free radical trapping experiments. The intermediates of LEV were determined by LC-MS and the possible degradation pathway was speculated in combination with density functional theory calculation, involving defluorination, decarboxylation, quinolone rings opening, and piperazine moieties oxidation reactions. It provides an advanced strategy for the fabrication of high-efficiency CQD-based Z-scheme photocatalysts for environmental remediation.

Environmental Implication

Chromium(VI) (Cr(VI)), a highly toxic metal ion, generally co-exists with organic pollutants in industrial effluents. The clean and effective technology for water purification is an imperative issue but still a challenging task. This work provides an advanced strategy for the fabrication of high-efficiency CQD-based Z-scheme photocatalysts for environmental remediation.

Graphic abstract
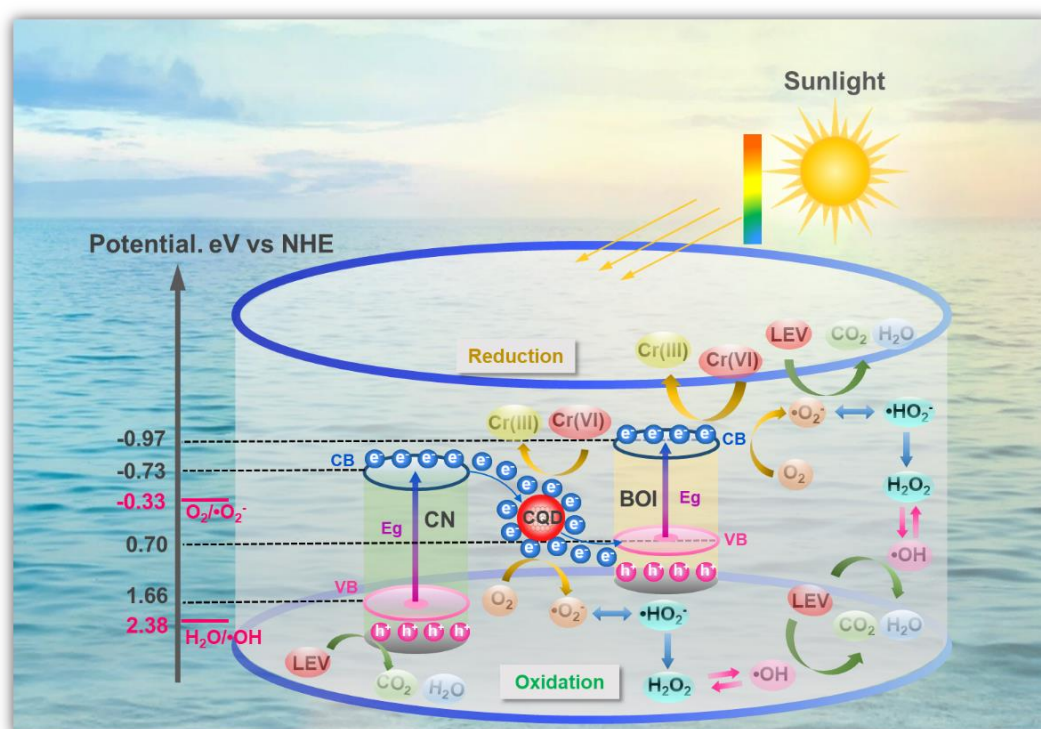
Highlights

- The Z-scheme $Bi_7O_9I_3$/g-C_3N_4 heterojunction was modified by lignin-derived CQD through a facile hydrothermal method.

- CQD/$Bi_7O_9I_3$/g-C_3N_4 exhibited superior photocatalytic activity for synchronous removal of Cr (VI) and organic pollutants.

- CQD acted as an electron reservoir to build a bridge between $Bi_7O_9I_3$ and g-C_3N_4, inhibiting the recombination of electron-hole pairs.

- $\cdot O^{2-}$ and holes were identified to be the dominant active species during the photocatalytic degradation of levofloxacin.

Fabrication of Z-scheme $Bi_7O_9I_3$/g-C_3N_4 heterojunction modified by carbon quantum dots for synchronous photocatalytic removal of Cr (Ⅵ) and organic pollutants

Lingli Zhu[a], Dekui Shen[a,*], Huiyan Zhang [a,*], Kai Hong Luo[b], Chong Li[c]

[a] Key Laboratory of Energy Thermal Conversion and Control of Ministry of Education, School of Energy and Environment, Southeast University, Nanjing 210096, PR China.

[b] Department of Mechanical Engineering, University College London, London WC1E7JE, U.K.

[c] School of Chemical Engineering, Dalian University of Technology, Dalian 116024, Liaoning, P.R. China

*Corresponding Author

E-mail address: 101011398@seu.edu.cn (D. Shen); hyzhang@seu.edu.cn (H. Zhang)

Abstract: Chromium(VI) (Cr(VI)), a highly toxic metal ion, generally co-exists with organic pollutants in industrial effluents. The clean and effective technology for water purification is an imperative issue but still a challenging task. The $Bi_7O_9I_3$/g-C_3N_4 (BOI/CN) composite modified by lignin-derived carbon quantum dots (CQD) was fabricated by hydrothermal method and applied for synchronous photocatalytic removal of Cr (Ⅵ) and levofloxacin (LEV). Compared to those of BOI (51.2%), CN (36.8%) and BOI/CN (74.4%), the photoreduction efficiency of Cr(VI) reached up to 100% by 0.5-CQD/BOI/CN photocatalyst (0.5% content of CQD) under 60 min of light irradiation, together with 94.8 % degradation efficiency of LEV. The redox potential in the Z-scheme CQD/BOI/CN system was estimated based on the band structure analysis, revealing that CQD as an electron reservoir constructed a bridge for promoting the electron transfer in BOI/CN heterojunction. The degradation of LEV was dominantly controlled by active species (holes and $\cdot O_2^-$) identified by electron paramagnetic resonance analysis and free radical trapping experiments. The intermediates of LEV were determined by LC-MS and the possible degradation pathway was speculated in combination with density functional theory calculation, involving defluorination, decarboxylation, quinolone rings opening, and piperazine moieties oxidation reactions. This work provides an advanced strategy for the fabrication of high-efficiency CQD-based Z-scheme photocatalysts for environmental remediation.

1. Introduction

Industrial effluents containing toxic heavy metal ions and organic chemical compounds from electroplating, metal finishing, leather tanning and steel fabricating pose a growing health risk and ecological threat [1, 2]. Among them, soluble hexavalent chromium (Cr(VI)) and residual antibiotics are of particular environmental concern owing to their mobility, carcinogenicity and teratogenicity on the ecological cycle chain [3, 4]. The traditional treatments including chemical precipitation, electrocatalysis, membrane separation, ion exchange, adsorption and bioremediation, suffer from the tedious operation, secondary pollution, low efficiency and high cost [5, 6]. Recently, the photocatalysis has emerged as a sustainable and promising purification technology due to its clean, green and convenient advantages [7]. For the effective removal of heavy metal and organic pollutants, it is of great significance to develop desirable photocatalysts with strong light harvesting capacity and photocatalytic activity.

In a variety of photocatalytic materials (TiO$_2$, C$_3$N$_4$, Fe$_2$O$_3$, ZnO, WO$_3$, etc.) [8-11], bismuth-based semiconductors like bismuth oxide, bismuthate, and bismuth halide oxide are emerging as a hot topic of research due to tunable band structure and abundant crystal forms [12, 13]. Among them, Bi$_7$O$_9$I$_3$ (BOI) possesses the unique structure of interchanging halogen atomic layer and [Bi$_2$O$_2$]$^{2+}$ layer, exhibiting rapid charge transfer and strong visible light absorption ability [14]. However, the pure BOI generally suffers from photocorrosion and electron-hole pairs recombination, leading to a low photocatalytic efficiency [12, 15]. The construction of BOI-based heterojunction structure has been verified to be an effective strategy to solve these issues. The energy bands of different heterojunction materials are arranged interleaved so that the separation of electron-hole pairs is improved through the internal electrical field, band buckling and electrostatic effects [16, 17]. The suitable heterojunction structure could broaden the sunlight response range, and promote electron-hole pairs separation, thus improving the photocatalytic activity [18, 19]. It is critical to select a semiconductor that matches the BOI band to construct an effective heterojunction photocatalyst. Even so, the recombination effect in the heterojunction structure might still occur when electrons are clustered at the band edge positions [20]. Pt, Au and Ag are commonly introduced as a mediator in the heterojunction system to guide the electrons to the surface photocatalyst [21, 22]. However, noble metals are expensive and rare, limiting their large-scale applications.

66   Carbon quantum dots (CQD) have been employed as an ideal alternative to modify the
67   heterojunction due to its chemical inertness, excellent electron reservoir and transfer
68   properties [23-25]. Particularly, the green synthesis of CQD using renewable biomass has the
69   merits of non-toxicity, low cost, and environmental friendliness, which is a win-win strategy
70   for the rational disposal and value-added utilization of solid waste [26, 27]. Meanwhile, the
71   unique up- and down-conversion photoluminescence (PL) properties of CQD would broaden
72   the absorption region of sunlight and boost the utilization of solar energy [28, 29]. Many
73   attempts have been made on the CQD-modified photocatalysts and satisfactory outcomes
74   have been achieved, such as $CQD/BiOBr/CeO_2$ [13], $CQD/Bi_2WO_6/g\text{-}C_3N_4$ [14],
75    $CQD/BiVO_4/Ag_3PO_4$ [16], $CQD/BiVO_4/Bi_3TaO_7$ [21], etc. Notably, biomass-derived CQD
76   are rarely utilized in heterojunction systems, and the insightful mechanism of CQD impacts
77   needs to be further clarified.

78   In this work, the $Bi_7O_9I_3/g\text{-}C_3N_4$ (BOI/CN) heterojunction modified by different contents
79   of lignin-derived CQD were prepared via a facile hydrothermal method. The morphology,
80   structure, chemical composition, optical and photoelectrochemical properties of the prepared
81   photocatalysts were thoroughly investigated. The photocatalytic activity was estimated
82   through synchronous photoreduction of Cr (VI) and degradation of levofloxacin (LEV) under
83   simulated light irradiation. The photocatalytic mechanism was elucidated by the free radical
84   trapping experiment and electron paramagnetic resonance spectrometer (EPR) analysis. The
85   photodegradation pathways of LEV were proposed according to the analysis of liquid
86   chromatography-mass spectrometry (LC−MS) combined with density functional theory (DFT)
87   calculations.

88   # 2. Experimental section

89   ## 2.1 Materials and chemicals

90   The materials and chemicals was detailed in Text S1 (Supporting Information).

91   ## 2.2 Photocatalysts preparation

92   ### 2.2.1 Synthesis of lignin-derived CQD

93   CQD was synthesized through a modified method according to previous works [30, 31].
94   As illustrated in Scheme 1, 0.8 g of 1, 2, 4-triaminobenzene dihydrochloride (T-acid) and 0.8
95   g of alkali lignin (AL) were mixed in 240 mL of deionized water, which was continuously
96   magnetic stirred for 1 h at 90 ℃. The supernatant was obtained via vacuum filtration (1.0 μm)

97 and then kept at 200 ℃ for 12 h in a 300 mL Teflon-lined autoclave. After cooling to room

98 temperature, the water-soluble CQD solution was obtained by vacuum filtration (0.22 μm).

99 The CQD solution was purified overnight in a dialysis membrane (3000 Da) and vacuum

100 lyophilized to CQD powder.

101 *2.2.2 Synthesis of g-C₃N₄ and CQD/g-C₃N₄*

102 The g-C$_3$N$_4$ (CN) and CQD/g-C$_3$N$_4$ (CQD/CN) were synthesized through thermal

103 polymerization from melamine. 0.025 g of CQD and 5 g of C$_3$H$_6$O$_6$ were dispersed in an

104 ethanol solution and sonicated for 0.5 h. The mixed solution was vacuum dried at 60 °C and

105 ground uniformly into a crucible. It was subsequently subjected to heating in a muffle furnace

106 at 5 °C/min to 550 ℃ and maintained for 4 h. Naturally cooled to ambient temperature, the

107 solid product was ground into uniform powder in a crucible and noted as CQD/CN. The CB

108 powder was obtained by heating C$_3$H$_6$O$_6$ directly in the muffle furnace without the addition of

109 CQD.

110 *2.2.3 Synthesis of Bi₇O₉I₃ and Bi₇O₉I₃-based composites*

111 The synthesis process of Bi$_7$O$_9$I$_3$ (BOI) and BOI-based composites were fabricated via a

112 hydrothermal method. 4.368 g of Bi(NO$_3$)$_3$·5H$_2$O was dispersed into 120 mL EG and

113 sonicated for 30 min to get solution A. 1.494 g of KI, g of CN, and a designed amount of

114 CQD was taken into 120 mL ethyl alcohol (EG) with sonicating for 30 min to get solution B.

115 Afterwards, solution A was manually mixed into solution B with stirring for 2 h. The obtained

116 solution was then treated in a 300 mL Teflon-lined autoclave at 160 ℃ for 24 h. The resulting

117 solution was centrifugalized at high speed and cleaned four times with DI water. The

118 CQD/BOI/CN powers were acquired through vacuum drying at 70 °C for 12 h. The contents

119 of CQD to Bi$_7$O$_9$I$_3$/g-C$_3$N$_4$ (BOI/CN) composite was controlled at 0.2 wt%, 0.5 wt% and 1

120 wt%, which were dvenoted as 0.2-CQD/BOI/CN, 0.5-CQD/BOI/CN, and 1.0-CQD/BOI/CN,

121 respectively. The pure BOI, BOI/CN, and CQD/Bi$_7$O$_9$I$_3$ (CQD/BOI) were obtained using the

122 above similar procedure in the absence of CN and CQD, CQD, CN, respectively.

Scheme 1. Schematic diagram of the synthetic route of the samples.

2.3 Characterization

The characterization of samples was detailed in Text S2, and photoelectrochemical measurement in Text S3 (Supporting Information).

2.4 Photocatalytic activity evaluation

2.4.1 Photocatalytic degradation and reduction

The photocatalytic activity of the synthesized photocatalysts was evaluated by photoreduction of Cr(VI) and degradation of LEV under 300 W Xe lamp irradiation (100 mW/cm^2, CEL-PF300-T6). As in each test, 50 mg of the photocatalyst was added in 100 mL of aqueous solution with Cr (VI) (20 mg/L) and LEV solution (20 mg/L). The mixed solution was next stirred continuously in the dark for 30 min. Afterwards, the solution was irradiated at 25 ℃ for 60 min. In the reaction process, 3 mL of the reactive solution was taken every 10 min and filtered through a 0.22 μm microporous membrane. The concentration of Cr(VI) in the supernatant was determined via the standard diphenylcarbazide (DPC) method (Text S4, Supporting Information). The concentration of LEV was recorded at λ_{max} = 279 nm using a UV-Vis spectrophotometer.

2.4.2 Recycling test

The photostability of the as-prepared photocatalysts was carried out through a series of consecutive recycling experiments. The spent samples samples were re-collected by

5

143　high-speed centrifugation, cleaned several times with deionized water, and dried at 80°C for

144　12 h before recycling. In addition, XRD and FT-IR analyses were also conducted for the used

145　materials to elucidate the photocatalytic activity loss during the recycling.

146　*2.5 Active species analysis*

147　　　　The EPR spectra were measured on a Bruker EMXplus-6/1 to identify the active species.

148　5, 5-dimethyl-1-pyrroline N-oxide (DMPO, 50 μL) was used as a spin capture reagent. The

149　active species were identified indirectly by free radical scavenging experiments with the

150　addition of reactive species scavenger in the photocatalytic process. The typical scavengers

151　employed were N_2 for the dissolved O_2, 1,4-benzoquinone (BQ, 1.0 mM) for the superoxide

152　radical ($\cdot O_2^-$), ethylene diamine tetraacetic acid disodium salt dihydrate (EDTA-2Na, 10 mM)

153　for the holes (h^+), isopropanol (IPA, 10 mM) for the hydroxyl radical ($\cdot OH$), respectively.

3.　Results and discussion

3.1 Morphology and structural characterization

156　　　　The morphology of the fabricated photocatalysts was observed by SEM. In Fig. 1a, the

157　pure BOI exhibits stacked 3D layered flower-like microspheres ranging from approximately

158　1~2 μm in diameter. This unique morphology facilitates the transfer of electrons and the

159　adsorption of contaminants. In Fig. 1b, the CN sample possesses a plicated lamellar structure

160　and would tend to stack and agglomerate due to high-temperature polymerization. In term of

161　BOI/CN (Fig. 1c) and CQD/BOI (Fig. 1d), CN and CQD are irregularly scattered on the

162　surface of BOI spheres. The smoothness of the composite surface is substantially lower than

163　that of the pure BOI. The CQD/CN (Fig. 1e) and CN have almost identical bulk morphology.

164　In Fig. 1f, the surface of 0.5-CQD/BOI/CN is coated with CN and CQD, resulting in a more

165　curved and rough surface. This indicates that nanocomposites have been successfully

166　prepared.
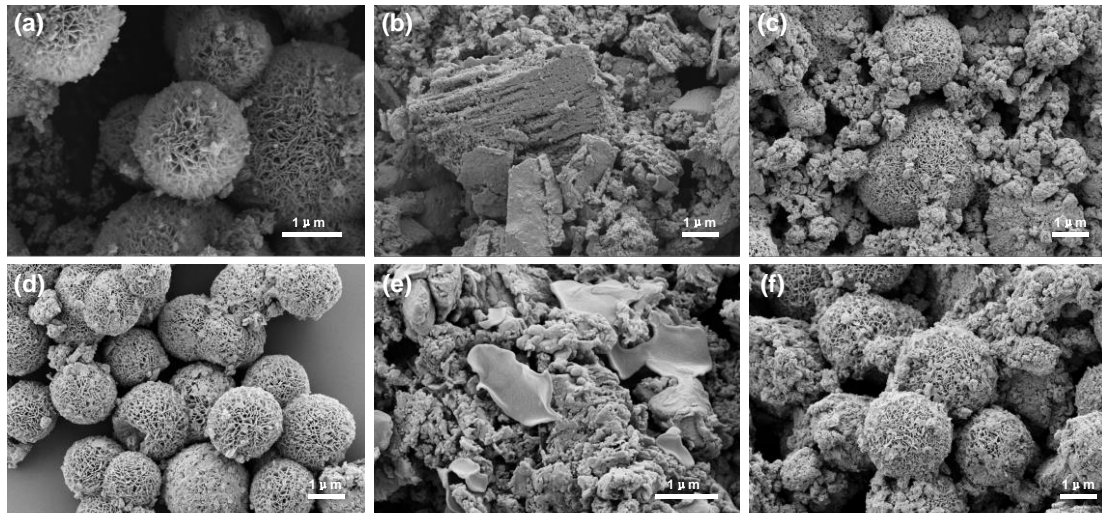
Fig. 1. SEM images of (a) BOI, (b) CN, (c) BOI/CN, (d) CQD/BOI, (e) CQD/CN, and (f) 0.5-CQD/BOI/CN.

The TEM and HR-TEM images further revealed the internal structure and lattice of the photocatalysts. As shown in Fig. 2a, the CQD are well-dispersed, 0-dimensional quasi-spherical spheres with sizes less than 10 nm. The lattice spacing of CQD in the inset is around 0.32 nm corresponding to the (0 0 2) diffraction plane of graphitic carbon. Fast Fourier transform (FFT) image obtained from the HR-TEM image confirms the presence of hexagonal diffraction planes of sp2 graphitic C in the inner regions of CQD. The TEM image of BOI in Fig. 2b presents a distinct flower-like nanoflake, and the pristine CN in Fig. 2c possesses an amorphous structure. The TEM image of CQD/BOI in Fig. 2d exhibit that the small-sized CQD are attached to the surface of the BOI nanoflowers with no change in the size and morphology. For 0.5-CQD/BOI/CN nanocomposite (Fig. 2e), the structures of CN and BOI are coupled together, and CQD nanoparticles are attached to the surface (Fig. 2f). The close contact between CQD, CN and BOI contributes to charge transfer during the photocatalytic reaction. Furthermore, the TEM mapping (Fig. 2g-n) shows that 0.5-CQD/BOI/CN nanocomposite contains C, N, O, Cl, I, and Bi, all of which could be apparently detected. The detailed content of each element is listed in Table S1 (Supporting Information), where the content of C, N and Cl increases with the proportion of CQD modifications. These outcomes further confirm that ternary CQD/BOI/CN/ photocatalysts are successfully prepared.

189
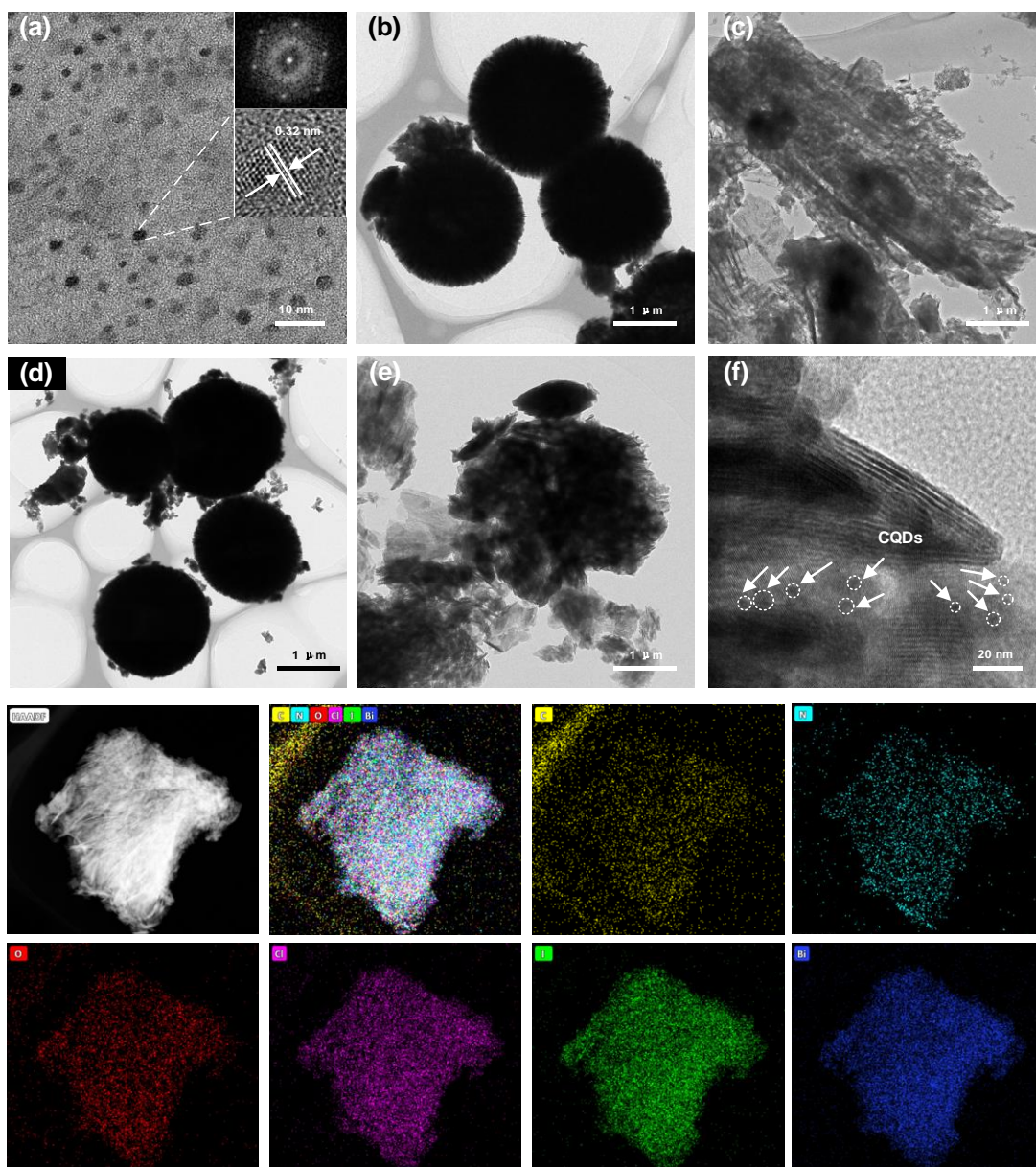
Fig. 2. TEM images of (a) CQD (Inset is the FFT pattern and lattice spacing), (b) BOI, (c) CN, (d) CQD/BOI, (e) 0.5-CQD/BOI/CN.

The crystal features of the fabricated photocatalysts were characterized by XRD. In Fig. 3a, within the range of 10–80°, CQD shows a broad peak centred at 26.7°, which is ascribed to (0 0 2) planes of graphitic carbon. The pure BOI has distinct characteristic peaks at 29.2°, 32.2°, 46.1°, and 55.6°, which are attributed to the (1 0 2), (1 1 0), (2 0 0), and (2 1 2) crystal planes (JCPDS 40-0548) [12], respectively. The pure CN possesses a weak diffraction peak at 13.2° and another sharp peak around 27.6°, which denotes the (1 0 0) and (0 0 2) plane of aromatic compounds and the stacked conjugated aromatic systems (JCPDS 87–1526), respectively. For BOI/CN, CQD/BOI and CQD/CN, the characteristic peaks of BOI and CN

in the binary composites can be apparently seen, while the flat peak of CQD in the nanocomposites is very insignificant due to its low level. The ternary composite CQD/BOI/CN exhibits distinctive three-part characteristic peaks belonging to BOI, CN and CQD, respectively. As the CQD content increases from 0.2% to 1.0%, the (0 0 2) lattice plane peak is strengthened, suggesting more coupling of the CQD to the BOI and CN [32]. Fig. 3b showed FT-IR spectra of the as-prepared photocatalysts for comparison. The broad characteristic absorption band at 3440-3280 cm^{-1} is assigned to stretching vibrations of O-H for CQD. The stretching vibration band at 3280-3087, 1766, 1603, 1399, and 1122 cm^{-1} are related to N-H, C=O, C=C, C-O, and C-N bonds [30, 31]. For pure BOI, the vibration bands at 3420, 1593, 1380, 1066, 881, and 507 cm^{-1} are characteristic of O-H, H-O-H bonds of adsorbed H_2O, I-O-I, Bi-O, and I-O bonds, respectively [17, 21]. The CN exhibits a broad peak at 3600-3000 cm^{-1}, which is assigned to the N-H bond originating from incompletely condensed N-H bonds or residual hydrogen atoms bound to the edges of graphite-like CN. The stretching vibration bands at 1670-1122 and 804 cm^{-1} belong to C=N and C-N bonds [33]. Similar characteristic bands are well traced in FT-IR spectra of BOI/CN, CQD/BOI, CQD/CN and CQD/BOI/CN, which further proves that the successful preparation of the binary and ternary nanocomposites. In comparison, the intensity of the stretching vibrations of carboxyl groups in CQD/BOI/CN is gradually strengthened with the increase of CQD content.
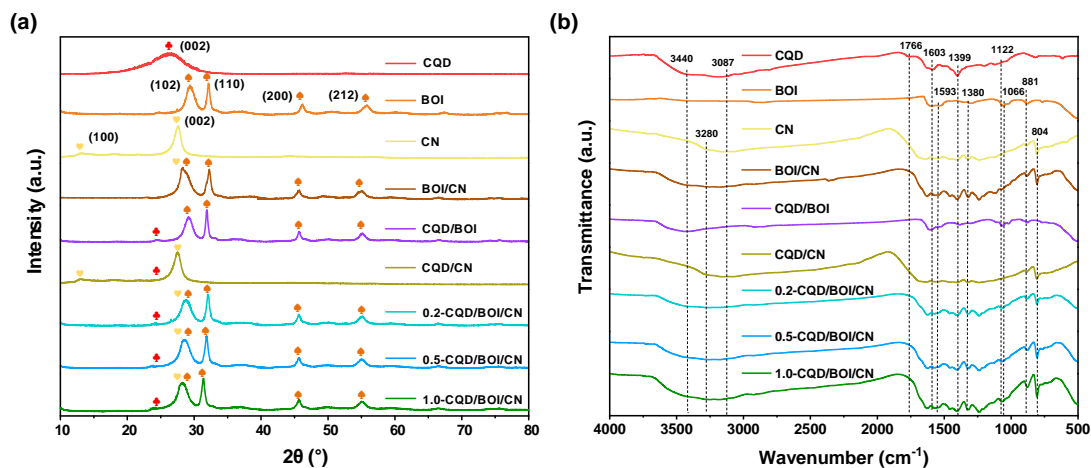
Fig. 3. XRD patterns and FTIR spectra of the fabricated photocatalysts.

XPS spectra were adopted to analyze the chemical compositions on the surface of the photocatalysts. Fig. 4a demonstrates the survey spectra including C 1s, N 1s, Cl 2p, Bi 4f, O 1s, and I 3d of the as-prepared photocatalysts. The C 1s spectra in Fig. 4b can be divided into characteristic peaks at 288.7 eV (C=O), 286.1 eV (C-O/C-N), 284.8 eV (C-C/C=C) for CQD, and 288.0 eV (N-C=N), 284.8 eV (C-C/C=C) for CN [34, 35]. The N 1s spectra in Fig. 4c

227   show three peaks of C-N-H, N-(C)$_3$, and C=N-C at 401.6, 400.2, and 398.8 eV for CQD and

228   CN [36]. The interaction of the N atoms in CQD/BOI/CN and certain species through

229   chemical bonding or intense electrostatic gravitational forces may cause a shift in the position

230   of the N 1s peak. The shift in binding energy implies the transfer of electrons from BOI to CN

231   and CQD at the interface [12]. The Cl 2p spectra in Fig. 4d are fitted into two peaks of Cl

232   2p$_{3/2}$, Cl 2p$_{1/2}$ at 199.6 and 198.2 eV originated from CQD. The Cl 2p peaks of CQD-based

233   nanocomposites are unapparent on account of the low content of CQD. The Bi 4f spectra in

234   Fig. 4e display two peaks at 163.9 eV (Bi 4f$_{5/2}$) and 158.9 eV (Bi 4f$_{7/2}$) for BOI-based

235   nanocomposites [13]. The O 1s spectra in Fig. 4f are fitted into two peaks at 532.9 eV (C=O)

236   and 531.4 eV (C-O) for CQD, and 531.8 eV (surface chemisorbed H$_2$O/OH$^-$), 530.3 eV (Bi-O

237   in [Bi$_2$O$_2$]$^{2+}$ slabs) for BOI [12, 37, 38]. The I 3d spectra in Fig.4g display two obvious peaks

238   at 630.4 eV (I 3d$_{3/2}$) and 618.8 eV (I 3d$_{5/2}$) in BOI-based nanocomposites, indicating that the

239   valence of I in BOI is -1 [12, 15]. The above findings prove the interconnection between CQD,

240   BOI and CN structures in the ternary nanocomposites, which benefits the electron transfer

241   and improve the photocatalytic performance.

242
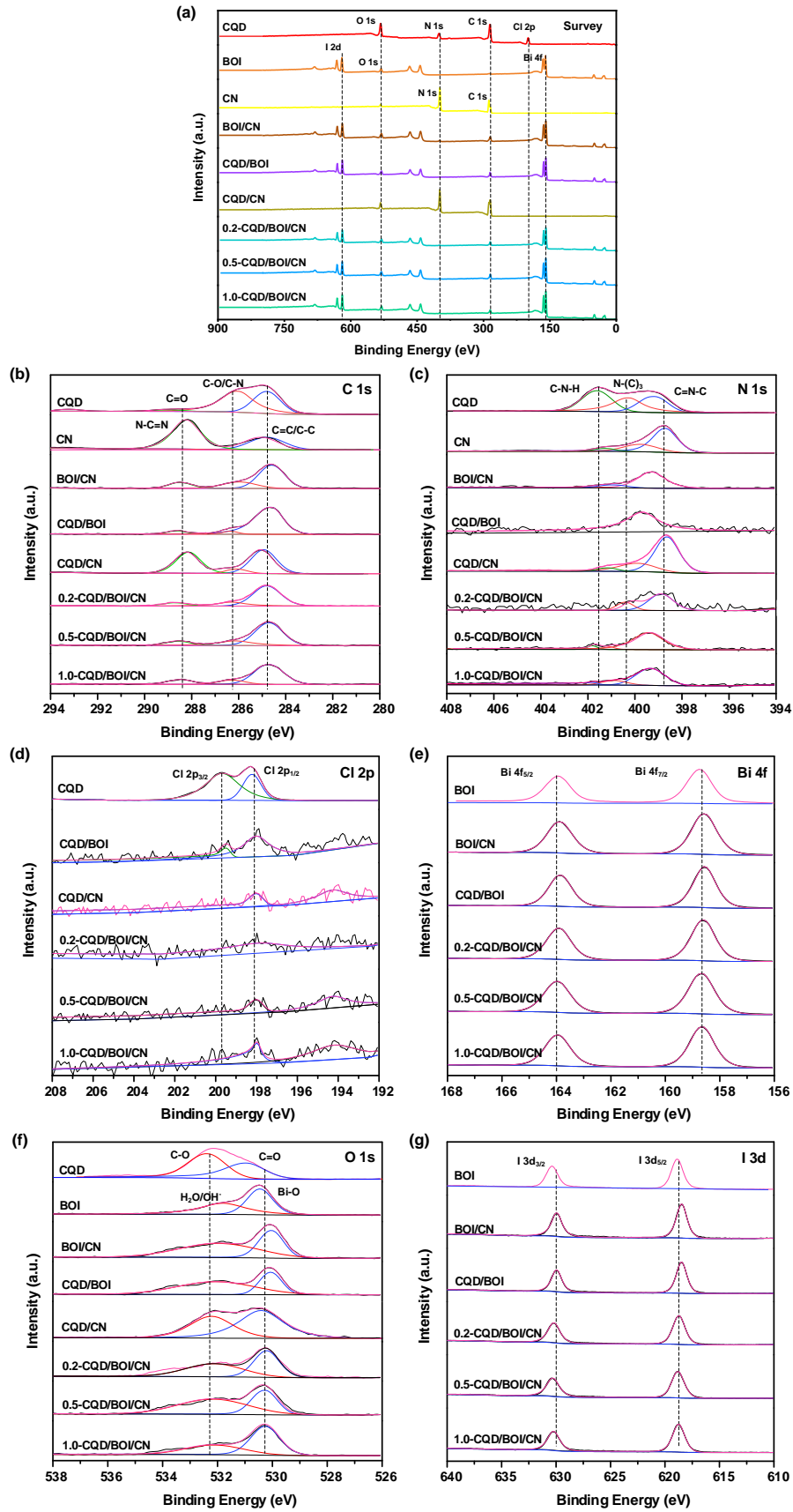
Fig. 4. (a) XPS survey spectra, high-resolution XPS spectra of (b) C1s, (c) N 1s, (d) Cl 2p, (e)

Bi 4f, (f) O 1s, and (g) I 3d of the as-prepared photocatalysts.

11

3.2 Optical and photoelectrochemical properties

The actual colour of all the photocatalysts can be seen in Fig. 5a, the modified nanocomposites are darker than the pristine photocatalysts. Particularly, the colour of the CQD/BOI/CN nanocomposites deepened as the CQD content varied from 0 to 1.0%. UV-vis DRS spectra in Fig. 5b display that CQD have an absorption edge of ~650 nm and two characteristic peaks at 261.4 and 489.9 nm, which are corresponding to π-π* transition of sp^2 conjugated structure and n-π* transitions of heteroatom doping defects, respectively [39]. The absorption boundaries of BOI, BOI/CN, CQD/BOI and CQD/BOI/CN are close to each other around 605.0-656.8 nm, while that of CN and CQD/CN are relatively narrow at 467.2 and 483.4 nm, limiting their photocatalytic efficiency. CQD/BOI possesses the broadest light absorption range, and all BOI-based nanocomposites have a satisfactory visible light response. Compared to BOI, CN and BOI/CN, CQD/BOI, CQD/CN and CQD/BOI/CN composites display the strengthened light-harvesting capacity with the addition of CQD, especially in response to ultraviolet and near-infrared light. The CQD/BOI/CN has a slight blue shift with increasing CQD content and the absorption intensity is mildly diminished. It is probably due to the interfacial interactions that hinder the light absorption. Nevertheless, the light absorption capacity is not the exclusive factor influencing the photocatalytic activity. The energy bandgaps (E_g) of photocatalysts are calculated by Eq. (1) [40]:

$$\alpha h\nu = A(h\nu - E_g)^{n/2} \tag{1}$$

Where α, hν, and A are absorption coefficients, photon energy and constant, respectively. The E_g is estimated by extrapolation of a plot of (αhν)$^{1/2}$ versus hν as displayed in Fig. 5c. The E_g of BOI, CN, CQD/BOI, and CQD/CN are calculated to be 1.67, 2.39, 1.61 and 2.27 eV, suggesting a narrowing of E_g after the introduction of CQD.

The PL emission behavior of CQD was explored under different excitation wavelengths. In Fig. 5d, when excited by the short-wavelength light from 400 to 600 nm, CQD presents a slight red shift from long-wavelength emission of 542 to 600 nm. This down-conversion PL of CQD can extend multiple photons to the near infrared region, thus thus improving the utilization of sunlight and achieving a full spectrum response. The PL spectra of the fabricated photocatalysts in Fig. 5e show that the 0.5-CQD/BOI/CN has the most pronounced fluorescence quenching, revealing the lowest recombination rate of photogenerated carriers [9, 41]. Besides, the PL intensity of CQD/BOI, CQD/CN and CQD/BOI/CN are weaker than that of the pure BOI, CN and BOI/CN. The results indicate that the introduction of CQD enables to inhibit the recombination of photogenerated carriers. In Fig. 5f, all the photocatalysts have regular photocurrent responses when the light is turned on or off. Their photocurrent intensity

are in the order of 0.5-CQD/BOI/CN > 1.0-CQD/BOI/CN > 0.2-CQD/BOI/CN > BOI/CN > CQD/BOI > CQD/CN >BOI >CN > CQD. The introduction of conductive CQD to BOI, CN or BOI/CN heterojunction considerably increases the electron lifetime and current separation efficiency [42, 43]. The electrochemical impedance spectra (EIS) was measured to further illustrate the interfacial electron transfer rate of the samples (Fig. 5g). Among them, 0.5-CQD/BOI/CN possesses the smallest arc radius of impedance curve, representing the fastest interfacial charge transfer [44]. The constructed CQD/BOI/CN composites with rapid electron transfer rate and effective carriers separation efficiency are qualified to participate in the photocatalytic reaction. Furthermore, VBXPS spectra (XPS valence band in Fig. S1, Supporting Information) were conducted to quantitatively depict the band structure of the as-prepared photocatalysts. The energy of the conduction band (E_{CB}) and valence band (E_{VB}) position can be determined by Eq. (2).

$$E_{CB} = E_{VB} - E_g \tag{2}$$

With the introduction of CQD, the E_{CB} of CQD/BOI (-0.84 eV) and CQD/CN (-0.75 eV) show a gradually downward shift from that of BOI (-0.95 eV) and CN (-0.85 eV), respectively. The E_{CB} level reveals the photoreduction ability of the photocatalysts (Fig. 5h) [15, 34].
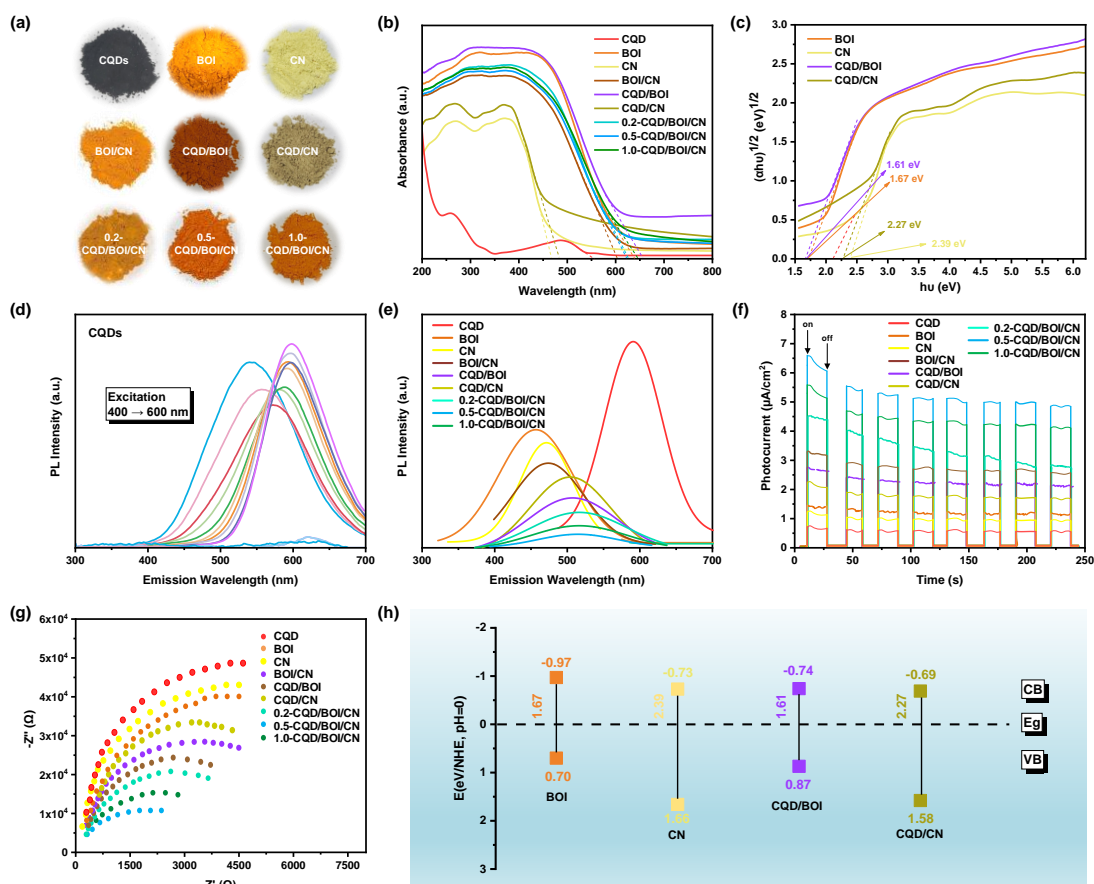
Fig. 5. (a) Photographs, (b) UV–vis DRS spectra, and (c) energy bandgaps of the as-prepared photocatalysts. (d) Down-convertion PL spectra of CQD. (e) PL spectra, (f) transient photocurrent response, (g) EIS and (h) band structure diagram of the as-prepared photocatalysts.

The photothermal effect as an assistant factor to facilitate photocatalytic activity, involves the transformation of photon energy into thermal energy [22]. The photothermal materials like metal and carbon materials, function as heat emitters at the reaction interface. The thermal energy of materials is in turn dissipated to the surrounding solution. In general, an elevated reaction temperature could lower the apparent activation energy in the photocatalytic system and thereby improve the photocatalytic performance [45, 46]. Hence, the surface temperature of the prepared photocatalysts was recorded by an infrared thermal imager to quantitatively analyze the photothermal effect. All the samples were subjected to a Xe lamp irradiation at 0, 1, 5, and 15 min for the Thermo images (Fig. S2, Supporting Information). As illustrated in Fig. 6a-d, the surface temperature of BOI/CN composite significantly increases from ambient temperature (28.5 ℃) to 52.4 ℃ within 1 min of irradiation, and slowly increases to 56.0 ℃ within 15 min of irradiation. While the surface temperature of 0.5-CQD/BOI/CN increases sharply from 28.7 to 71.2 ℃ within 1 min of irradiation, and gradually increases to 79.6 ℃ within 15 min of irradiation. In the photocatalytic process, there are two dominant sources of heat: the direct thermal radiation from the light source as well as the intrinsic photothermal effect of the sample. The thermal variations induced by the external light irradiation are constant. The thermal increment of BOI/CN composites can be attributed to the external light source. The sudden increase in thermal energy of 0.5-CQD/BOI/CN may be due to the synergy and SPR effect of CQD and Bi, which contributes to the photothermal effect [12, 22].
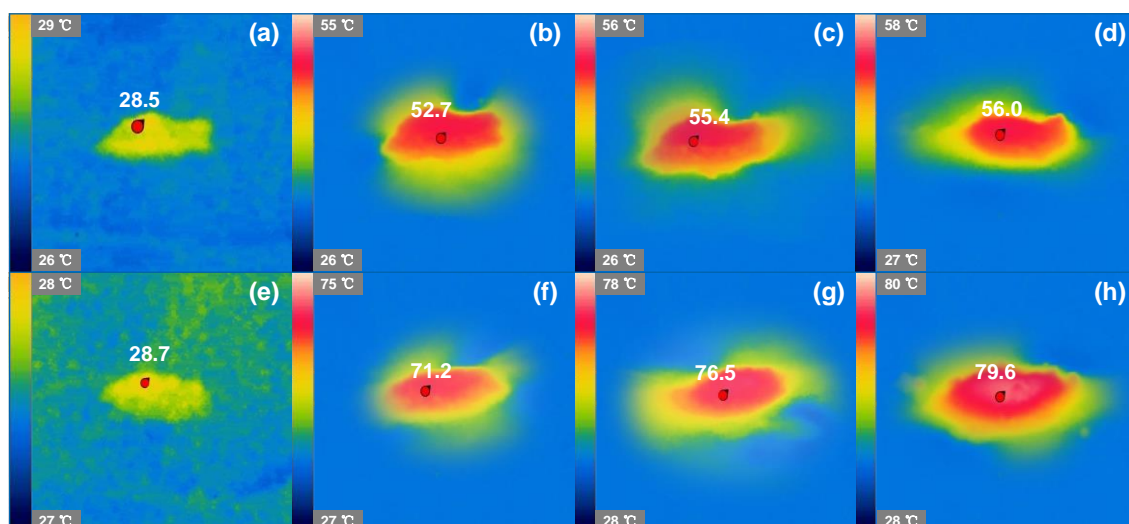
Fig. 6. Thermographic images of (a-d) BOI/CN and (e-h) 0.5-CQD/BOI/CN composites under light irradiation of 0, 1, 5 and 15 min, respectively.

3.3 Photocatalytic activity evaluation

The photocatalytic activity of the fabricated photocatalysts was estimated for synchronous removal of Cr (VI) and LEV under 300W Xe lamp irradiation. In Fig. 7a, the monomer photocatalysts of CQD, BOI, and CN exhibit limited reduction efficiency of 4.5%, 51.2%, and 36.8% after 60 min of light irradiation, which may be attributed to the intensive photon scattering and rapid charge recombination. The binary nanocomposites of CQD/BOI, CQD/CN and BOI/CN present higher reduction efficiency of 64.1%, 41.6% and 74.4% due to the improved charges separation efficiency. The construction of ternary heterojunctions CQD/BOI/CN can further enhance the photocatalytic performance for the Cr (VI) removal with the optimal reduction efficiency up to 100% (0.5-CQD/BOI/CN). The photocatalytic reduction kinetics for the photocatalysts are fitted with a pseudo-first-order kinetic model [13, 47, 48]:

$$-ln(C/C_0) = kt \tag{3}$$

Where k is the kinetic reaction rate (min^{-1}). The linear kinetic curves of the Cr(VI) reduction over the photocatalysts are depicted in Fig. 7b. The 0.5-CQD/BOI/CN possesses the highest Cr(VI) reduction rate of 0.08725 min^{-1}, corresponding to 164.3, 9.3,15.2 6.4, 12.7, 4.8, 2.8, and 2.4 times higher than that of CQD (0.00053 min^{-1}), BOI (0.00939 min^{-1}), CN (0.00575 min^{-1}), CQD/BOI (0.01357 min^{-1}), CQD/CN (0.00689 min^{-1}), BOI/CN (0.01825 min^{-1}), 0.2-CQD/BOI/CN (0.03099 min^{-1}), 1.0-CQD/BOI/CN (0.03671 min^{-1}), respectively. The excessive accumulation of CQD on the surface of BOI/CN nanocomposite would inevitably hinder the charge transfer and active sites, with consequently lowering the photoreduction

15

347 efficiency. As seen in Fig. 7c, the photoreduction efficiency of 0.5-CQD/BOI/CN for Cr(VI)
348 maintains 79% after the five times recycling cycle experiments. Additionally, XRD patterns
349 and FT-IR spectra of 0.5-CQD/BOI/CN before and after five recycle experiments are
350 measured (Fig. S3, Supporting Information). In comparison, there are no emerging peaks and
351 significant shifts appeared, suggesting the invariant crystalline structure and surface
352 functional groups of the reused 0.5-CQD/BOI/CN.

353   As for the synchronous photocatalytic degradation of LEV (Fig. 7d), all the
354 photocatalysts achieve the adsorption-desorption equilibrium after constant stirring for 30 min
355 in the darkness. The blank sample has negligible degradation capacity of LEV (20 mg L^{-1}).
356 Comparatively, the binary nanocomposites of CQD/BOI (62.5%), CQD/CN (36.8%), and
357 BOI/CN (74.4%) exhibit higher LEV degradation efficiency than the monomer photocatalysts
358 of CQD (4.5%), BOI (39.8%), CN (26.8%) after irradiation for 60 min. The constructed
359 ternary 0.5-CQD/BOI/CN heterojunction shows the optimal LEV degradation efficiency of
360 94.8%, which is in accordance with the optical and photoelectrochemical results. In Fig. 7e,
361 the maximum reaction rate over 0.5-CQD/BOI/CN (0.03863 min^{-1}) is about 72.9, 6.2, 9.9
362 times higher than the monomer photocatalysts of CQD (0.00053 min^{-1}), BOI (0.00626 min^{-1}),
363 CN (0.00389 min^{-1}), and 3.1, 6.7, 2.2 times higher than the binary photocatalysts of CQD/BOI
364 (0.01262 min^{-1}), CQD/CN (0.00575 min^{-1}), BOI/CN (0.0174 min^{-1}). It is noteworthy that the
365 introduction of insufficient and excessive CQD negatively affects the further improvement of
366 photoreaction and degradation efficiency [33, 49, 50]. The reusability of the photocatalyst is
367 vital for the application in practice, and the five photocatalytic cycling experiments were
368 performed. In Fig. 7f, the degradation efficiency of 0.5- CQD/BOI/CN for LEV decrease to
369 77% after the fifth cyclic experiment. These results manifest the superior recyclability and
370 stability of the as-synthesized photocatalysts.

371
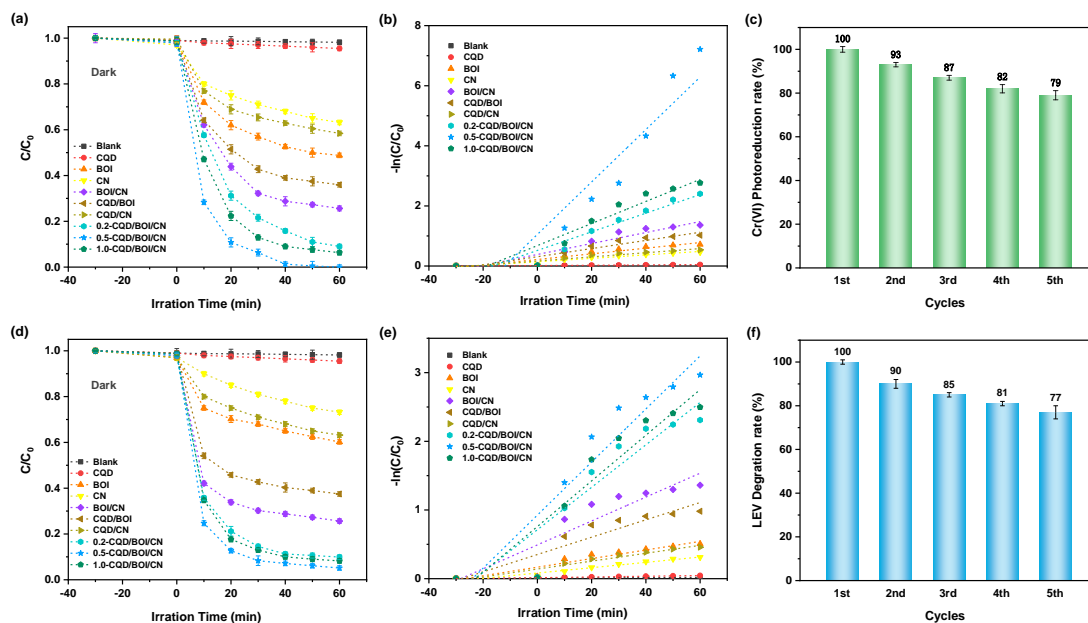
Fig. 7. (a) Photoreduction of Cr(VI) by different photocatalysts (C_0=20 mg L^{-1}). (b) The pseudo-first-order reaction kinetics. (c) Reusability evaluation in cycling experiment of Cr(VI) photoreduction. (d) Photodegradation of LEV by different photocatalysts (C_0=20 mg L^{-1}). (e) The pseudo-first-order reaction kinetics. (f) Reusability evaluation in cycling experiment of LEV degradation.

3.4 Photocatalytic reaction mechanism

To gain insight into the photocatalytic reaction mechanism, EPR measurement was performed under simulated sunlight irradiation to determine the free radical species. The characteristic quartets with intensities of 1:2:2:1 and 1:1:1:1 are corresponding to DMPO-•OH and DMPO-•O$_2^-$ signals, respectively. In Fig. 8a, b, the pure BOI and BOI/CN composite both exhibit very weak peaks of DMPO-•OH and DMPO-•O$_2^-$ signals under light irradiation. As the introduction of CQD, the significant characteristic peaks of the two signals are observed for CQD/BOI nanocomposite (Fig. 8c). In comparison, 0.5-CQD/BOI/CN nanocomposite presents apparently stronger signals of both DMPO-•OH and DMPO-•O$_2^-$ (Fig. 8d). The generation process of active species can be clarified through the investigation on energy band structure. The electrons in the CB of BOI seem to have the potential to reduce O$_2$ to •O$_2^-$, since the E_{CB} (-0.97 eV) position is lower than that of •O$_2^-$ (-0.13 eV vs NHE). But the rapid recombination of photogenerated electrons and holes in pure BOI hinders the generation of free radicals, resulting in poor photocatalytic performance. BOI/CN exhibits a typical type II heterojunction with building a dual transfer mechanism, where electrons transfer migrate from the CB of BOI to CN and holes migrate from the VB of CN to BOI.

17

394 This traditional model shows the limited generation of active species due to higher E_{CB} of CN
395 than BOI, and lower E_{VB} of BOI than CN. The accepted redox ability of BOI/CN
396 heterojunction is mainly ascribed to efficient electron-hole pairs separation rather than active
397 species. In CQD/BOI nanocomposite, CQD as an electron reservoir significantly facilitates
398 the efficient separation of photogenerated electron holes. The enriched electrons in the surface
399 of CQD and the CB of CQD/BOI (-0.84 eV) can be both used for the reduction reaction
400 accompanied by promoting the generation of $\bullet O_2^-$. The VB of CQD/BOI cannot oxidize H_2O
401 to $\bullet OH$ as its E_{VB} (0.87 eV) position is lower than that of $H_2O/\bullet OH$ (2.38 eV vs NHE). The
402 separated electrons, holes, $\bullet O_2^-$ and $\bullet OH$ (from the weak secondary reaction) are responsible
403 for the strengthened photocatalytic activity of CQD/BOI. As for 0.5-CQD/BOI/CN, the
404 photoexcited electrons migrate from the CB of CN to the VB of BOI via CQD as a bridge.
405 Then, the electrons in the CB of BOI (-0.97 eV) and holes in the VB of CN (1.54 eV) can be
406 used for photocatalytic reduction and oxidation. The accelerated electronic transfer by CQD
407 and lower CB position dramatically enhances the generation of $\bullet O_2^-$ and $\bullet OH$ from the
408 secondary reaction. Therefore, 0.5-CQD/BOI/CN processes superior photocatalytic
409 performance.
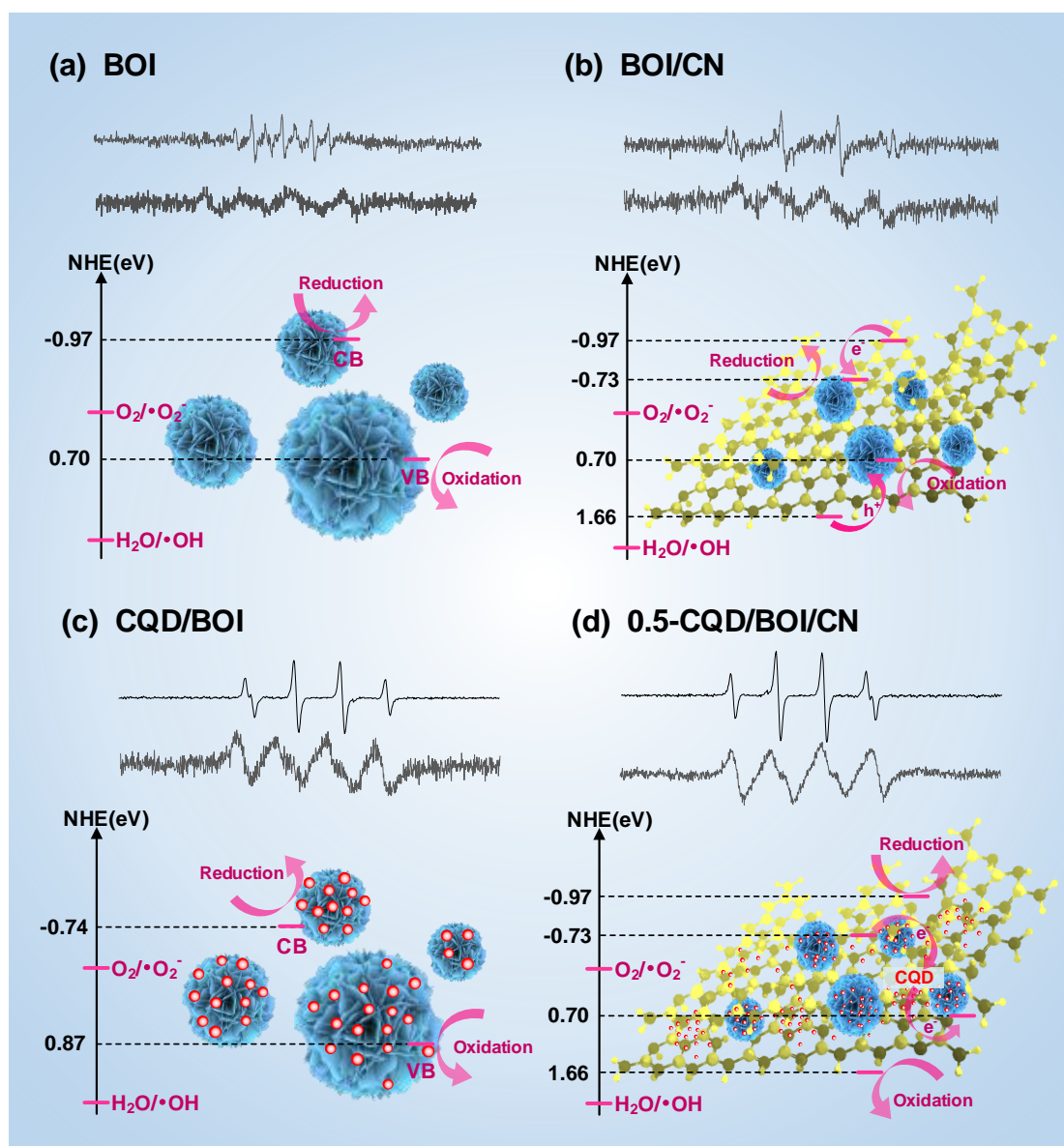
Fig. 8. EPR spectra and the energy band structures of (a) BOI, (b) BOI/CN, (c) CQD/BOI, and (d) 0.5-CQD/BOI/CN photocatalysts.

The EPR spectra of different CQD/BOI/CN composites in Fig. 9a manifest that the characteristic peak intensity of DMPO-•OH increases and then decreases as the CQD content ranges from 0.2% to 1.0% under light irradiation. The situation of DMPO-•O$_2^-$ is consistent with that of •OH (Fig. 9b), and the 0.5-CQD/BOI/CN composite shows the optimal intensity of both DMPO-•OH and DMPO-•O$_2^-$ signals. It is known that the photoexcited •OH and •O$_2^-$ radicals are essential for the photocatalytic activity of CQD/BOI/CN composite, whereas excessive or insufficient CQD content has a negative impact on the generation of active

species. It is consistent with the experimental results of the photocatalytic performance evaluation. According to the EPR analysis, the LEV degradation by 0.5-CQD/BOI/CN mainly relied on the h^+, $\bullet O_2^-$, $\bullet OH$, and the Cr(VI) reduction only relied on the electrons. The active species trapping experiments were implemented to further identify the contribution of each free radical. In Fig. 9c, the addition of IPA, BQ and EDTA-2Na trapping agent has a minor effect on the photoreduction reaction. 0.5-CQD/BOI/CN with $Na_2S_2O_3$ added exhibits the lowest removal rate of 38.6%, revealing that e^- is the only dominant factor in the photoreduction of Cr (VI). In Fig. 9d, the degradation rate of LEV over 0.5-CQD/BOI/CN is slightly decreased from 99.9% to 90.5% in the presence of IPA ($\bullet OH$ scavenger), while observably declined to 47.2%, 36.8%, 41.2% with the BQ ($\bullet O_2^-$ scavenger), EDTA-2Na (h^+ scavenger) and N_2 (dissolved O_2 scavenger). It is confirmed that $\bullet O_2^-$ and h^+ are the dominant reactive radicals for the degradation process of LEV, and dissolved O_2 can be photoreduced by e^- to yield $\bullet O_2^-$ radicals for attacking the LEV molecules.
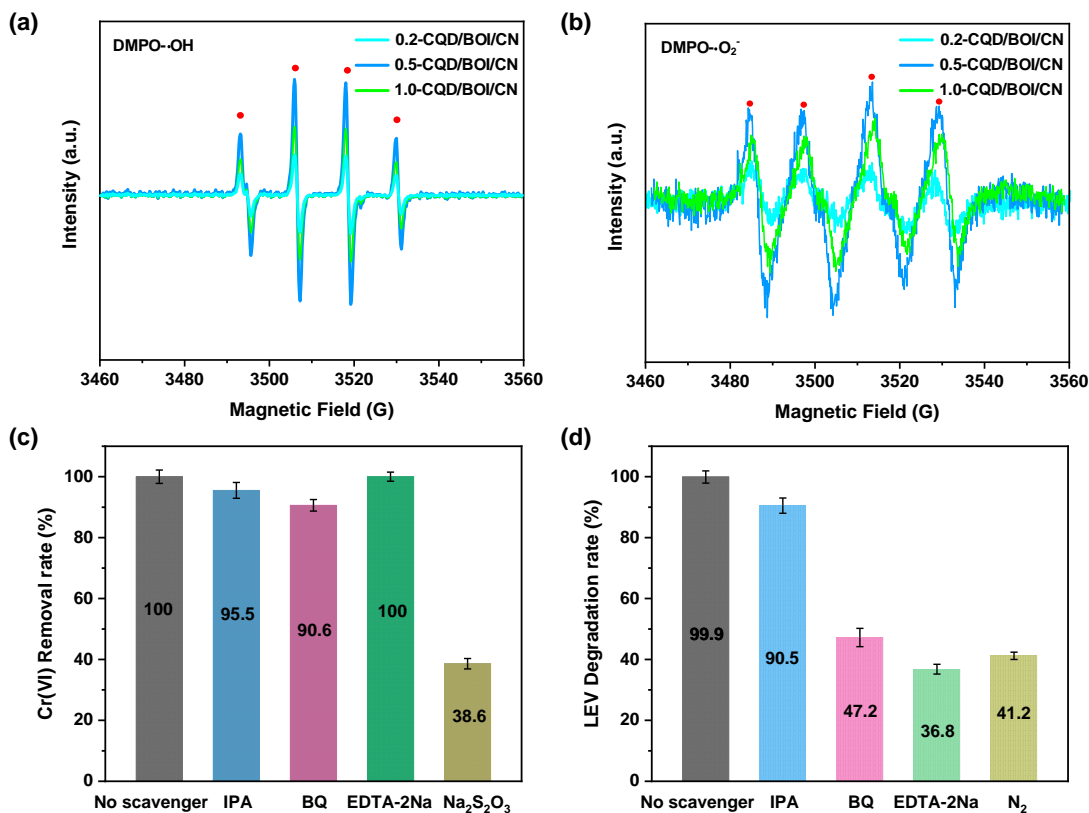

Fig. 9. EPR spectra using DMPO to capture (a) $\bullet OH$ and (b) $\bullet O_2^-$ over different CQD/BOI/CN composites. Active species trapping experiment of 0.5-CQD/BOI/CN

437 photocatalyst during the reduction of (d) Cr (VI) and degradation of (c) LEV.

438

439   Accordingly, the potential photocatalytic mechanism of the 0.5-CQD/BOI/CN composite
440 is proposed and illustrated in Fig. 10. The excellent photocatalytic performance of
441 0.5-CQD/BOI/CN may be ascribed to the fabrication of Z-scheme heterojunction. The BOI
442 and CN are photoexcited under the sunlight irradiation, producing electrons and holes at their
443 CBs and VBs, separately. As CQD processes outstanding electrons collect and transfer ability,
444 the electrons in the CB of CN first migrate to the CQD surface. Then, the electrons on CQD
445 allow quick recombination with the holes on the VB of BOI. CQD act as an electron reservoir
446 or buffer to build a bridge between the CB of CN and the VB of BOI. This Z-scheme system
447 can both accelerate the rate of electron transfer and effectively inhibit the recombination of
448 electron-hole pairs inside BOI and CN. Thus, exceptionally high yields of electrons and holes
449 are formed in the CB of BOI and the VB of CN, which can be directly used in photo-redox
450 reactions. The CB position (-0.97 eV) of BOI is more negative than that of $O_2/\bullet O_2^-$ (-0.33 eV
451 vs NHE), while the VB of CN is not more positive than $H_2O/\bullet OH$ (2.38 eV vs NHE). The
452 enriched electrons in the CB of BOI can reduce the adsorbed O_2 to $\bullet O_2^-$ ($O_2 + e^- \rightarrow \bullet O_2^-$), and
453 then to $\bullet HO_2^-$, H_2O_2, and $\bullet OH$ from the secondary reaction ($\bullet O_2^- + e^- + H^+ \rightarrow \bullet HO_2^-$, $\bullet HO_2^- +$
454 $H^+ \rightarrow H_2O_2$, $H_2O_2 \leftrightarrow 2\bullet OH$) [18, 51]. Noteworthily, the above structural analysis has verified
455 the N, Cl co-doping of CQD, so the electrons accumulated on the surface of CQD could
456 reduce Cr(VI) and activate O_2 to yield plentiful active species owing to its abundant surface
457 defect sites. The organic pollutants (LEV) can be attacked by these active species ($\bullet O_2^-$, $\bullet OH$)
458 and holes, eventually oxidized to CO_2 and H_2O. The electrons, holes and active species can be
459 sustainably refreshed by the sunlight irradiation, leading to highly efficient photocatalytic
460 redox capability of 0.5-CQD/BOI/CN composite.

461
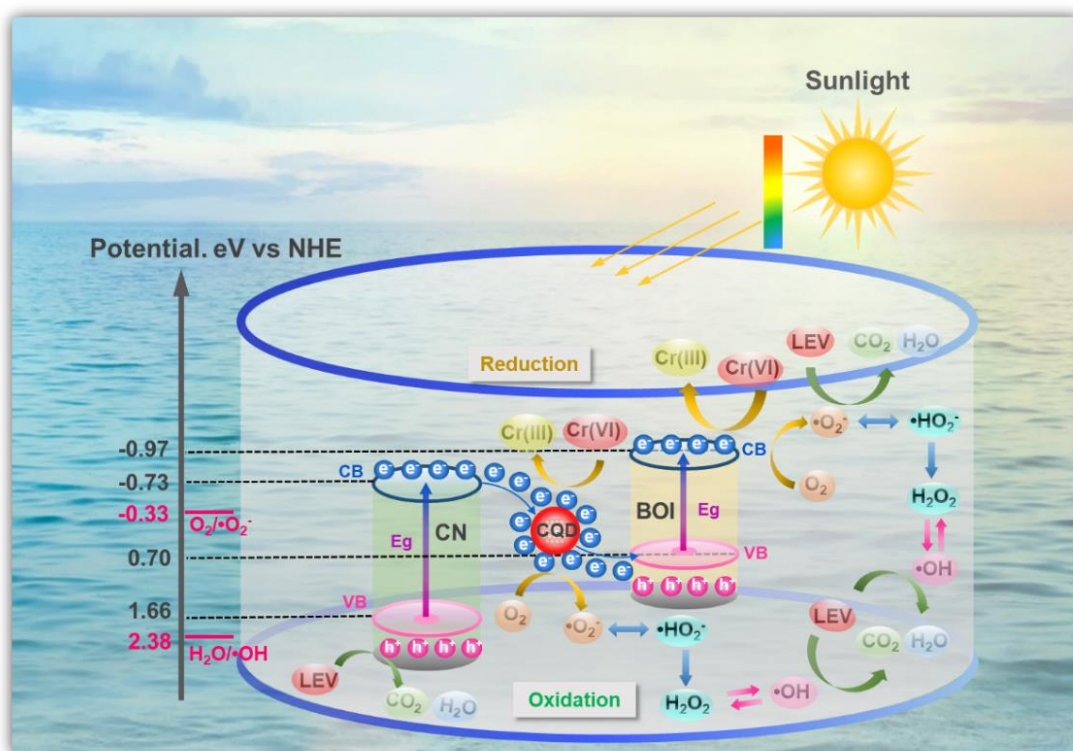
Fig. 10. Schematic diagram illustrating the possible photocatalytic mechanism for the synchronous reduction of Cr(VI) and degradation of LEV by 0.5-CQD/BOI/CN photocatalyst.

3.5 Photocatalytic degradation pathway

DFT calculations (method in Text S5) were employed to explore the charge distribution of organic pollutant. The chemical structure of LEV molecule is described in Fig. 11a. The highest occupied molecular orbital (HOMO) and the lowest unoccupied molecular orbital (LUMO) in Fig. 11b represent the ability to lose electron and the deficient-electron sites of LEV molecule, respectively [52, 53]. Combined with the electrostatic potential (ESP) profile (Fig. 11c) on the molecular surface of LEV, the peripheral regions of N19 and N23 are susceptibly attacked by positive holes, while O11, O13, O14 and F26 tend to be attacked by anionic radicals ($•O_2^-$), promoting of molecular interface reactions [54]. The natural population analysis (NPA) charge distribution and Fukui index of LEV were calculated to quantitatively evaluate reactive sites of electrophilic, nucleophilic, and radical attacking [54-56]. From Fig. 11d, C8 and O11 in a quinolone ring exhibit the highest f^0 values of 0.0642 and 0.0634. Meanwhile, C9 connected to a carboxyl group, has the high f^- and f^0 of 0.0385 and 0.0393. It implies that the quinolone ring is vulnerable to decarboxylation and cleavage by electrophilic $•O_2^-$ attack. The high Fukui index values of N19 ($f^- = 0.0958$, $f^0 = 0.0534$) and N23 ($f^- = 0.041$, $f^0 = 0.0216$) make piperazine epoxidation feasible. The high f^0 values of 0.0271 and 0.0265 for C11 and F26 are crucial for defluorination reaction. The f^-

22

and f^0 values of C4, C1, C3 and O18 are also high, contributing to the all-cleavage of LEV molecules to small molecules.

Atom	q(N)	q(N+1)	q(N-1)	f^-	f^+	f^0
1(C)	-0.0518	-0.1031	-0.0116	0.0402	0.0513	0.0457
2(C)	0.0849	0.0468	0.101	0.0161	0.0381	0.0271
3(C)	0.0251	-0.0164	0.0448	0.0197	0.0416	0.0306
4(C)	0.0491	0.0006	0.1009	0.0518	0.0485	0.0502
5(C)	0.0198	0.0115	0.0352	0.0153	0.0083	0.0118
6(C)	-0.0295	-0.0357	-0.0021	0.0274	0.0062	0.0168
7(N)	-0.0071	-0.0431	0.0099	0.0171	0.0359	0.0265
8(C)	0.0408	-0.0697	0.0586	0.0178	0.1105	0.0642
9(C)	-0.0616	-0.1001	-0.0216	0.0401	0.0385	0.0393
10(C)	0.1151	0.0557	0.1265	0.0114	0.0594	0.0354
11(O)	-0.28	-0.368	-0.2413	0.0387	0.088	0.0634
12(C)	0.2001	0.1739	0.2119	0.0118	0.0263	0.019
13(O)	-0.3079	-0.3542	-0.273	0.0348	0.0463	0.0406
14(O)	-0.165	-0.1889	-0.151	0.0141	0.0239	0.019
15(C)	0.0384	0.0318	0.0427	0.0043	0.0067	0.0055
16(C)	0.035	0.0239	0.0441	0.0091	0.0112	0.0101
17(C)	-0.0757	-0.084	-0.0679	0.0078	0.0084	0.0081
18(O)	-0.1266	-0.152	-0.0967	0.0299	0.0254	0.0276
19(N)	-0.0752	-0.0862	0.0206	0.0958	0.011	0.0534
20(C)	-0.0077	-0.0128	0.0093	0.017	0.0051	0.011
21(C)	-0.0088	-0.0126	0.0087	0.0175	0.0038	0.0106
22(C)	-0.0116	-0.0152	0.0007	0.0123	0.0036	0.008
23(N)	-0.1082	-0.1103	-0.0671	0.041	0.0021	0.0216
24(C)	-0.0116	-0.0165	0.003	0.0146	0.0049	0.0097
25(C)	-0.0411	-0.0467	-0.0258	0.0153	0.0056	0.0104
26(F)	-0.0949	-0.1272	-0.0743	0.0207	0.0322	0.0265

Fig. 11. DFT calculations on LEV molecule. (a) LEV chemical structure. (b) HOMO and LUMO. (c) ESP-mapped molecular surface of LEV. (d) NPA and Fukui index of LEV.

To elucidate the photocatalytic oxidation process of the target pollutants, LC−MS was further performed to determine the intermediate products. The major chemical formula, m/z, and possible structure are listed in Fig. S4 and Table S2. On the basis, four feasible photocatalytic degradation pathways of LEV are deduced in Fig. 12, primarily involving defluorination, decarboxylation, quinolone rings cleavage, and piperazine moieties oxidation [54, 57, 58]. In Path I, the initial substrate LEV (m/z 362) is attacked by active species (h+, •O_2^- and •OH) and L1 (m/z 360) is formed with the replacement of the F group by a hydroxyl group. The quinolone moieties are further oxidized to product L2 (m/z 392) and then ring is opened to yield products L3 (m/z 322), L4 (m/z 233), and L5 (m/z 188) [59, 60]. Product L2 could also be decarboxylated and then take off the piperazine ring to obtain L8 (m/z 290), L9 (m/z 262), and L10 (m/z 232). The second and third degradation paths are the demethylation and decarboxylation from LEV to yield L12 (m/z 348) and L19 (m/z 318), respectively. The subsequent deamination reaction results in the loss of quinolone ring to obtain L14 (m/z 278) and L15 (m/z 233) [61, 62]. The fourth degradation path refers to the piperazine epoxidation and ring cleavage to obtain product L20 (m/z 392). The aldehyde groups of L20 are removed to product L23 (m/z 279) and the F group is simultaneously substituted with a hydroxyl group to product L15 (m/z 233) [63]. Then L15 undergoes the dehydration reaction to product L16 (m/z 217) and the quinolone rings are further destroyed under the continuous oxidation [64].

504 Ultimately, these intermediates are mineralized to small organic molecules, CO_2 and H_2O via

505 deep oxidation reaction [65], and the photocatalytic degradation of the LEV on

506 0.5-CQD/BOI/CN composite is achieved.
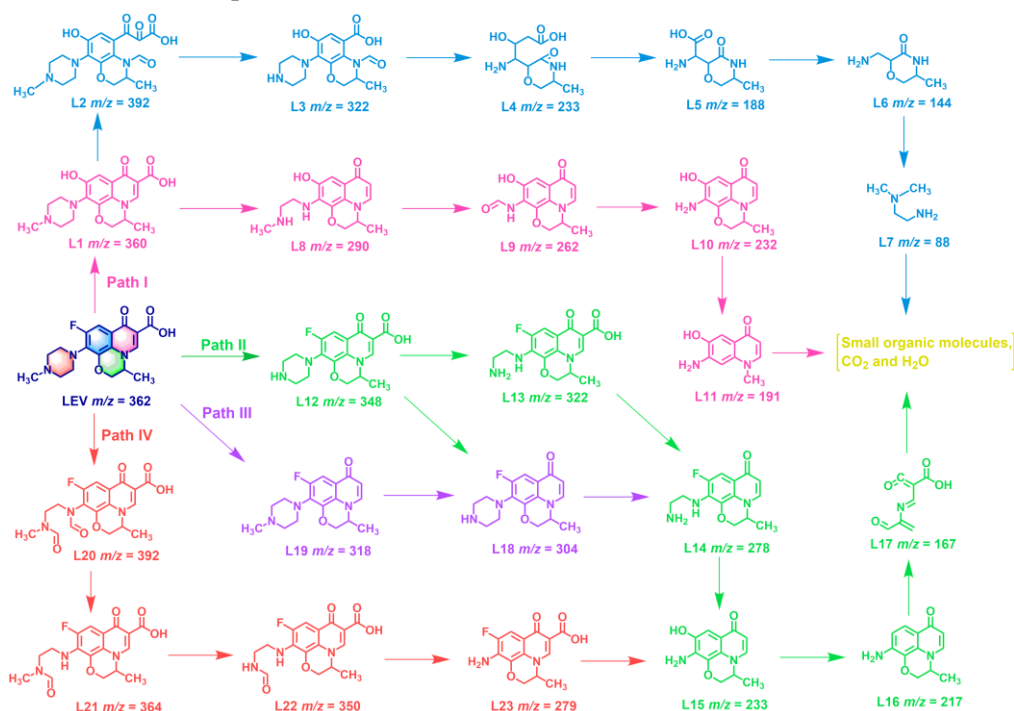
508 **Fig. 12.** The possible degradation pathways of LEV in the 0.5-CQD/BOI/CN system.

4. Conclusions

510   A series of UV-vis-light-driven Z-scheme CQD/BOI/CN composites were successfully

511 synthesized by the hydrothermal method. The optimal composite (0.5-CQD/BOI/CN) features

512 the broadened UV-vis light absorption region, highly effective photogenerated carrier

513 separation and enhanced redox ability. The photoreduction efficiency of Cr (VI) is up to 100 %

514 over 0.5-CQD/BOI/CN under 60 min of light irradiation, and its reaction rate (0.08725 min^{-1})

515 is about 4.8 times higher than that of BOI/CN (0.01825 min^{-1}). The synergetic degradation

516 efficiency of LEV reaches 94.8 % under 60 min of light irradiation, and the reaction rate

517 (0.03863 min^{-1}) is 2.2 times higher than that of BOI/CN (0.0174 min^{-1}). CQD sandwiched

518 with BOI/CN heterogeneous interface acts as an electron reservoir, facilitating the efficient

519 separation of photogenerated electron-hole pairs and accelerating the charge transfer. The

520 down-conversion PL property of CQD is conducive to broadening the UV-vis light absorption

521 region. It was found that LEV degradation was dominantly controlled by the holes and $\bullet O_2^-$

522 regarding to the free radical trapping experiments and EPR analysis. According to the DFT

523 calculation and LC-MS analysis, the decomposition pathway of LEV involves the

524 defluorination, decarboxylation, quinolone rings opening, and piperazine moieties oxidation

reactions. This work provides a promising approach to synthesize the CQD-based Z-scheme photocatalysts for synergistic removal of Cr(VI) and organic pollutants for efficient water purification.

Declaration of Competing Interest

The authors declare that they have no known competing financial interests or personal relationships that could have appeared to influence the work reported in this paper.

Acknowledgements

Appendix A. Supplementary data

Supplementary data to this article can be found online at

References

[1] J. Wu, J. Wang, Y. Du, H. Li, Y. Yang, X. Jia, Chemically controlled growth of porous CeO_2 nanotubes for Cr(VI) photoreduction, Applied Catalysis B: Environmental. 174-175 (**2015**) 435-444.

[2] X. Zheng, T. Liu, J. Wen, X. Liu, Flower-like Bi2S3-In2S3 heterojunction for efficient solar light induced photoreduction of Cr(VI), Chemosphere. 278 (**2021**) 130422.

[3] Z. Guo, W. Wei, Y. Li, Z. Li, F. Hou, A. Wei, Cr(VI)-imprinted polymer wrapped on urchin-like Bi_2S_3 for reduced photocorrosion and improved photoreduction of aqueous Cr(VI), J Hazard Mater. 422 (**2022**) 126946.

[4] L. Jia, X. Tan, Y. Li, Y. Zhang, S. Cao, W. Zhou, X. Huang, L. Liu, T. Yu, Design of $BiOBr_{0.25}I_{0.75}$ for synergy photoreduction Cr(VI) and capture Cr(III) over wide pH range, Chinese Chemical Letters. 33 (**2022**) 3053-3060.

[5] B. Valizadeh, T.N. Nguyen, S. Kampouri, D.T. Sun, M.D. Mensi, K. Stylianou, B. Smit, W.L. Queen, A novel integrated Cr(vi) adsorption–photoreduction system using MOF@polymer composite beads, Journal of Materials Chemistry A. 8 (**2020**) 9629-9637.

[6] P. Wang, T. Song, C. Xie, P. Yang, 2D/2D Co-Al layered double hydroxide/TiO2 heterostructures for photoreduction of Cr (VI), Applied Surface Science. 580 (**2022**).

558 [7] Y. Zhang, M. Xu, H. Li, H. Ge, Z. Bian, The enhanced photoreduction of Cr(VI) to Cr(III)
559   using carbon dots coupled TiO_2 mesocrystals, Applied Catalysis B-Environmental. 226
560   (**2018**) 213-219.

561 [8] Q. Zhang, L. Li, S. Wang, J. Shao, C. Liu, Y. Wang, G. Li, Chemically Homogenizing
562   MoO_2 Nanocrystals into Monodispersed Spherical Shapes for Enhanced Cr(VI)
563   Photoreduction, ACS Applied Nano Materials. 5 (**2022**) 9950-9957.

564 [9] W. Wang, Z. Zeng, G. Zeng, C. Zhang, R. Xiao, C. Zhou, W. Xiong, Y. Yang, L. Lei, Y.
565   Liu, D. Huang, M. Cheng, Y. Yang, Y. Fu, H. Luo, Y. Zhou, Sulfur doped carbon quantum
566   dots loaded hollow tubular g-C_3N_4 as novel photocatalyst for destruction of Escherichia
567   coli and tetracycline degradation under visible light, Chemical Engineering Journal. 378
568   (**2019**).

569 [10] Y. Zeng, D. Chen, T. Chen, M. Cai, Q. Zhang, Z. Xie, R. Li, Z. Xiao, G. Liu, W. Lv,
570   Study on heterogeneous photocatalytic ozonation degradation of ciprofloxacin by
571   TiO_2/carbon dots: Kinetic, mechanism and pathway investigation, Chemosphere. 227
572   (**2019**) 198-206.

573 [11] Y. Li, W. Xiang, T. Zhou, M. Huang, C. Wang, X. Wu, J. Mao, P. Wang, Visible light
574   induced efficient activation of persulfate by a carbon quantum dots (CQDs) modified
575   γ-Fe_2O_3 catalyst, Chinese Chemical Letters. 31 (**2020**) 2757-2761.

576 [12] Y. Yuan, R.T. Guo, L.F. Hong, Z.D. Lin, X.Y. Ji, W.G. Pan, Fabrication of a dual
577   S-scheme $Bi_7O_9I_3$/g-C_3N_4/Bi_3O_4Cl heterojunction with enhanced visible-light-driven
578   performance for phenol degradation, Chemosphere. 287 (**2022**) 132241.

579 [13] L. Liang, S. Gao, J. Zhu, L. Wang, Y. Xiong, X. Xia, L. Yang, The enhanced
580   photocatalytic performance toward carbamazepine by nitrogen-doped carbon dots
581   decorated on $BiOBr$/CeO_2: Mechanism insight and degradation pathways, Chemical
582   Engineering Journal. 391 (**2020**).

583 [14] X. Liu, Z. Yang, Y. Yang, H. Li, Carbon quantum dots sensitized 2D/2D carbon nitride
584   nanosheets/bismuth tungstate for visible light photocatalytic degradation norfloxacin,
585   Chemosphere. 287 (**2022**) 132126.

586 [15] J. Lai, X. Jiang, M. Zhao, S. Cui, J. Yang, Y. Li, Thickness-dependent layered $BiOIO_3$
587   modified with carbon quantum dots for photodegradation of bisphenol A: Mechanism,
588   pathways and DFT calculation, Applied Catalysis B: Environmental. 298 (**2021**).

589 [16] J. Zhang, M. Yan, X. Yuan, M. Si, L. Jiang, Z. Wu, H. Wang, G. Zeng, Nitrogen doped
590   carbon quantum dots mediated silver phosphate/bismuth vanadate Z-scheme photocatalyst
591   for enhanced antibiotic degradation, J Colloid Interface Sci. 529 (**2018**) 11-22.

592 [17] R. Xie, L. Zhang, H. Xu, Y. Zhong, X. Sui, Z. Mao, Construction of up-converting
593   fluorescent carbon quantum dots/Bi20TiO32 composites with enhanced photocatalytic
594   properties under visible light, Chemical Engineering Journal. 310 (**2017**) 79-90.

595 [18] V.D. Dang, J. Adorna, T. Annadurai, T.A.N. Bui, H.L. Tran, L.-Y. Lin, R.-A. Doong,
596   Indirect Z-scheme nitrogen-doped carbon dot decorated Bi_2MoO_6/g-C_3N_4 photocatalyst
597   for enhanced visible-light-driven degradation of ciprofloxacin, Chemical Engineering
598   Journal. 422 (**2021**).

599 [19] Z. Wang, Q. Cheng, X. Wang, J. Li, W. Li, Y. Li, G. Zhang, Carbon dots modified
600   bismuth antimonate for broad spectrum photocatalytic degradation of organic pollutants:
601   Boosted charge separation, DFT calculations and mechanism unveiling, Chemical

602   Engineering Journal. 418 (**2021**).

603 [20] P. Peng, Z. Chen, X. Li, Y. Wu, Y. Xia, A. Duan, D. Wang, Q. Yang, Biomass-derived
604   carbon quantum dots modified Bi_2MoO_6/Bi_2S_3 heterojunction for efficient photocatalytic
605   removal of organic pollutants and Cr (VI), Separation and Purification Technology. 291
606   (**2022**).

607 [21] S. Le, W. Li, Y. Wang, X. Jiang, X. Yang, X. Wang, Carbon dots sensitized 2D-2D
608   heterojunction of $BiVO_4/Bi_3TaO_7$ for visible light photocatalytic removal towards the
609   broad-spectrum antibiotics, Journal of Hazardous Materials. 376 (**2019**) 1-11.

610 [22] J. Zhang, M. Si, L. Jiang, X. Yuan, H. Yu, Z. Wu, Y. Li, J. Guo, Core-shell
611   Ag@nitrogen-doped carbon quantum dots modified BiVO4 nanosheets with enhanced
612   photocatalytic performance under Vis-NIR light: Synergism of molecular oxygen
613   activation and surface plasmon resonance, Chemical Engineering Journal. 410 (**2021**).

614 [23] M.H. Elsayed, J. Jayakumar, M. Abdellah, T.H. Mansoure, K. Zheng, A.M. Elewa, C. L.
615   Chang, L. Y. Ting, W. C. Lin, H.-h. Yu, W.-H. Wang, C. C. Chung, H. H. Chou,
616   Visible-light-driven hydrogen evolution using nitrogen-doped carbon quantum
617   dot-implanted polymer dots as metal-free photocatalysts, Applied Catalysis B:
618   Environmental. 283 (**2021**).

619 [24] Y. Liu, Y. Zhao, Q. Wu, X. Wang, H. Nie, Y. Zhou, H. Huang, M. Shao, Y. Liu, Z. Kang,
620   Charge storage of carbon dot enhances photo-production of H-2 and H_2O_2 over
621   Ni_2P/carbon dot catalyst under normal pressure, Chemical Engineering Journal. 409
622   (**2021**).

623 [25] Y. Wang, B.B. Chen, Y.T. Gao, L. Jiang, J. Lv, S. Chang, R.C. Qian, D.W. Li, Carbon
624   dots induced in-situ formation of porous europium micro-networks with enhanced
625   photocatalysis, J Colloid Interface Sci. 606 (**2022**) 600-606.

626 [26] M.W. Nugraha, N.H. Zainal Abidin, Supandi, N.S. Sambudi, Synthesis of tungsten oxide/
627   amino-functionalized sugarcane bagasse derived-carbon quantum dots (WO_3/N-CQDs)
628   composites for methylene blue removal, Chemosphere. 277 (**2021**) 130300.

629 [27] Z. Zhu, X. Li, M. Luo, M. Chen, W. Chen, P. Yang, X. Zhou, Synthesis of carbon dots
630   with high photocatalytic reactivity by tailoring heteroatom doping, J Colloid Interface Sci.
631   605 (**2021**) 330-341.

632 [28] Q. Wang, G. Wang, X. Liang, X. Dong, X. Zhang, Supporting carbon quantum dots on
633   NH_2-MIL-125 for enhanced photocatalytic degradation of organic pollutants under a
634   broad spectrum irradiation, Applied Surface Science. 467-468 (**2019**) 320-327.

635 [29] J. F. Li, C. Y. Zhong, J. R. Huang, Y. Chen, Z. Wang, Z. Q. Liu, Carbon dots decorated
636   three-dimensionally ordered macroporous bismuth-doped titanium dioxide with efficient
637   charge separation for high performance photocatalysis, Journal of Colloid and Interface
638   Science. 553 (**2019**) 758-767.

639 [30] L. Zhu, D. Shen, Q. Wang, K.H. Luo, Green Synthesis of Tunable Fluorescent Carbon
640   Quantum Dots from Lignin and Their Application in Anti-Counterfeit Printing, ACS
641   Applied Materials & Interfaces. (**2021**).

642 [31] L. Zhu, D. Shen, K. Hong Luo, Triple-emission nitrogen and boron co-doped carbon
643   quantum dots from lignin: Highly fluorescent sensing platform for detection of hexavalent
644   chromium ions, J Colloid Interface Sci. 617 (**2022**) 557-567.

645 [32] L. Zhu, D. Shen, Q. Liu, C. Wu, S. Gu, Sustainable synthesis of bright green fluorescent

646 carbon quantum dots from lignin for highly sensitive detection of Fe^{3+} ions, Applied
647 Surface Science. 565 (**2021**).

648 [33] J. Liu, H. Xu, Y. Xu, Y. Song, J. Lian, Y. Zhao, L. Wang, L. Huang, H. Ji, H. Li,
649 Graphene quantum dots modified mesoporous graphite carbon nitride with significant
650 enhancement of photocatalytic activity, Applied Catalysis B-Environmental. 207 (**2017**)
651 429-437.

652 [34] S. Xiong, S. Bao, W. Wang, J. Hao, Y. Mao, P. Liu, Y. Huang, Z. Duan, Y. Lv, D. Ouyang,
653 Surface oxygen vacancy and graphene quantum dots co-modified Bi2WO6 toward highly
654 efficient photocatalytic reduction of CO_2, Applied Catalysis B: Environmental. 305
655 (**2022**).

656 [35] A. Mahmood, G. Shi, Z. Wang, Z. Rao, W. Xiao, X. Xie, J. Sun, Carbon quantum
657 dots-TiO_2 nanocomposite as an efficient photocatalyst for the photodegradation of
658 aromatic ring-containing mixed VOCs: An experimental and DFT studies of adsorption
659 and electronic structure of the interface, J Hazard Mater. 401 (**2021**) 123402.

660 [36] Q. Li, S. Wang, Z. Sun, Q. Tang, Y. Liu, L. Wang, H. Wang, Z. Wu, Enhanced CH4
661 selectivity in CO_2 photocatalytic reduction over carbon quantum dots decorated and
662 oxygen doping g-C3N4, Nano Research. 12 (**2019**) 2749-2759.

663 [37] S.-R. Kim, W.-K. Jo, Boosted photocatalytic decomposition of nocuous organic gases
664 over tricomposites of N-doped carbon quantum dots, $ZnFe_2O_4$, and BiOBr with different
665 junctions, Journal of Hazardous Materials. 380 (**2019**).

666 [38] Y. Cui, T. Wang, J. Liu, L. Hu, Q. Nie, Z. Tan, H. Yu, Enhanced solar photocatalytic
667 degradation of nitric oxide using graphene quantum dots/bismuth tungstate composite
668 catalysts, Chemical Engineering Journal. 420 (**2021**).

669 [39] Y. Liu, H. Yang, C. Ma, S. Luo, M. Xu, Z. Wu, W. Li, S. Liu, Luminescent Transparent
670 Wood Based on Lignin-Derived Carbon Dots as a Building Material for Dual-Channel,
671 Real-Time, and Visual Detection of Formaldehyde Gas, ACS Appl Mater Interfaces. 12
672 (**2020**) 36628-36638.

673 [40] M. Zhu, M. Han, C. Zhu, L. Hu, H. Huang, Y. Liu, Z. Kang, Strong coupling effect at the
674 interface of cobalt phosphate-carbon dots boost photocatalytic water splitting, J Colloid
675 Interface Sci. 530 (**2018**) 256-263.

676 [41] Q. Si, W. Guo, H. Wang, B. Liu, S. Zheng, Q. Zhao, H. Luo, N. Ren, T. Yu, Difunctional
677 carbon quantum dots/g-C3N4 with in-plane electron buffer for intense tetracycline
678 degradation under visible light: Tight adsorption and smooth electron transfer, Applied
679 Catalysis B: Environmental. 299 (**2021**).

680 [42] H. Ming, D. Wei, Y. Yang, B. Chen, C. Yang, J. Zhang, Y. Hou, Photocatalytic activation
681 of peroxymonosulfate by carbon quantum dots functionalized carbon nitride for efficient
682 degradation of bisphenol A under visible-light irradiation, Chemical Engineering Journal.
683 424 (**2021**).

684 [43] F. Wang, Y. Wu, Y. Wang, J. Li, X. Jin, Q. Zhang, R. Li, S. Yan, H. Liu, Y. Feng, G. Liu,
685 W. Lv, Construction of novel Z-scheme nitrogen-doped carbon dots/{001} TiO2
686 nanosheet photocatalysts for broad-spectrum-driven diclofenac degradation: Mechanism
687 insight, products and effects of natural water matrices, Chemical Engineering Journal. 356
688 (**2019**) 857-868.

689 [44] X. Han, Q. Chang, N. Li, H. Wang, J. Yang, S. Hu, In-situ incorporation of carbon dots

28

into mesoporous nickel boride for regulating photocatalytic activities, Carbon. 137 (**2018**) 484-492.

[45] Y. Yuan, W.-g. Pan, R.-t. Guo, L.-f. Hong, Z.-d. Lin, X.-y. Ji, Flower spherical-like $Bi_7O_9I_3$/AgI S-scheme heterojunction for phenol photodegradation: The synergetic effect of dual surface plasmon resonance and photothermal property, Separation and Purification Technology. 297 (**2022**).

[46] Y. Yuan, R. Guo, L. Hong, X.-y. Ji, Z. Lin, Z. Li, W. Pan, A review of metal oxide-based Z-scheme heterojunction photocatalysts: actualities and developments, Materials Today Energy. 21 (**2021**).

[47] M. Ebrahimi, M. Samadi, S. Yousefzadeh, M. Soltani, A. Rahimi, T.-c. Chou, L.-C. Chen, K.-H. Chen, A.Z. Moshfegh, Improved Solar-Driven Photocatalytic Activity of Hybrid Graphene Quantum Dots/ZnO Nanowires: A Direct Z-Scheme Mechanism, ACS Sustainable Chemistry & Engineering. 5 (**2016**) 367-375.

[48] D. Pan, J. Jiao, Z. Li, Y. Guo, C. Feng, Y. Liu, L. Wang, M. Wu, Efficient Separation of Electron–Hole Pairs in Graphene Quantum Dots by TiO2 Heterojunctions for Dye Degradation, ACS Sustainable Chemistry & Engineering. 3 (**2015**) 2405-2413.

[49] A. Yuan, H. Lei, F. Xi, J. Liu, L. Qin, Z. Chen, X. Dong, Graphene quantum dots decorated graphitic carbon nitride nanorods for photocatalytic removal of antibiotics, Journal of Colloid and Interface Science. 548 (**2019**) 56-65.

[50] Y. Qu, X. Xu, R. Huang, W. Qi, R. Su, Z. He, Enhanced photocatalytic degradation of antibiotics in water over functionalized N,S-doped carbon quantum dots embedded ZnO nanoflowers under sunlight irradiation, Chemical Engineering Journal. 382 (**2020**).

[51] J. Cui, Y. Pei, J. Hou, Y. Zheng, Y. Zhang, K. Wei, X. He, B. Xi, Construction of a carbon dots-based Z-scheme photocatalytic electrode with enhanced visible-light-driven activity for Cr(VI) reduction and carbamazepine degradation in different reaction systems, Chemical Engineering Journal. 420 (**2021**).

[52] X. Gu, L. Zhu, D. Shen, C. Li, Facile synthesis of multi-emission nitrogen/boron co-doped carbon dots from lignin for anti-counterfeiting printing, Polymers (Basel). 14 (**2022**).

[53] L. Zhu, D. Shen, Q. Liu, K.H. Luo, C. Li, Mild Acidolysis-Assisted Hydrothermal Carbonization of Lignin for Simultaneous Preparation of Green and Blue Fluorescent Carbon Quantum Dots, ACS Sustainable Chemistry & Engineering. 10 (**2022**) 9888-9898.

[54] Y. He, J. Qian, P. Wang, J. Wu, B. Lu, S. Tang, P. Gao, Acceleration of levofloxacin degradation by combination of multiple free radicals via MoS_2 anchored in manganese ferrite doped perovskite activated PMS under visible light, Chemical Engineering Journal. 431 (**2022**).

[55] W. Liu, Y. Li, F. Liu, W. Jiang, D. Zhang, J. Liang, Visible-light-driven photocatalytic degradation of diclofenac by carbon quantum dots modified porous g-C_3N_4: Mechanisms, degradation pathway and DFT calculation, Water Research. 151 (**2019**) 8-19.

[56] Y. Duan, L. Deng, Z. Shi, X. Liu, H. Zeng, H. Zhang, J. Crittenden, Efficient sulfadiazine degradation via in-situ epitaxial grow of Graphitic Carbon Nitride (g-C_3N_4) on carbon dots heterostructures under visible light irradiation: Synthesis, mechanisms and toxicity evaluation, Journal of Colloid and Interface Science. 561 (**2020**) 696-707.

[57] T. Cao, J. Xu, M. Chen, Construction of 2D/0D direct Z-scheme $Bi_4O_5I_2$/Bi_3TaO_7

734   heterojunction photocatalysts with enhanced activity for levofloxacin degradation under

735   visible light irradiation, Separation and Purification Technology. 291 (**2022**).

736   [58] G. Fan, S. Yang, B. Du, J. Luo, X. Lin, X. Li, Sono-photo hybrid process for the

737   synergistic degradation of levofloxacin by $FeVO_4/BiVO_4$: Mechanisms and kinetics,

738   Environ Res. 204 (**2022**) 112032.

739   [59] F. Hasanvandian, A. Shokri, M. Moradi, B. Kakavandi, S. Rahman Setayesh,

740   Encapsulation of spinel $CuCo_2O_4$ hollow sphere in V_2O_5-decorated graphitic carbon

741   nitride as high-efficiency double Z-type nanocomposite for levofloxacin photodegradation,

742   J Hazard Mater. 423 (**2022**) 127090.

743   [60] S. Wang, M. Chen, S. Shen, C. Cheng, A. Cai, A. Song, X. Lu, G. Gao, M. Ma, Z. Zhang,

744   X. Xu, Bifunctionalized $Fe_7S_8@MoS_2$–O core-shell with efficient photocatalytic activity

745   based on internal electric field, Journal of Cleaner Production. 335 (**2022**).

746   [61] Z. Hu, M. Ge, C. Guo, Efficient removal of levofloxacin from different water matrices

747   via simultaneous adsorption and photocatalysis using a magnetic $Ag_3PO_4/rGO/CoFe_2O_4$

748   catalyst, Chemosphere. 268 (**2021**) 128834.

749   [62] S. Li, C. Wang, Y. Liu, B. Xue, W. Jiang, Y. Liu, L. Mo, X. Chen, Photocatalytic

750   degradation of antibiotics using a novel $Ag/Ag_2S/Bi_2MoO_6$ plasmonic p-n heterojunction

751   photocatalyst: Mineralization activity, degradation pathways and boosted charge

752   separation mechanism, Chemical Engineering Journal. 415 (**2021**).

753   [63] J. Shen, L. Qian, J. Huang, Y. Guo, Z. Zhang, Enhanced degradation toward

754   Levofloxacin under visible light with S-scheme heterojunction In_2O_3/Ag_2CO_3: Internal

755   electric field, DFT calculation and degradation mechanism, Separation and Purification

756   Technology. 275 (**2021**).

757   [64] S.L. Prabavathi, K. Saravanakumar, C.M. Park, V. Muthuraj, Photocatalytic degradation

758   of levofloxacin by a novel $Sm6WO_{12}/g-C_3N_4$ heterojunction: Performance, mechanism

759   and degradation pathways, Separation and Purification Technology. 257 (**2021**).

760   [65] X. Zhang, Y. Zhang, X. Jia, N. Zhang, R. Xia, X. Zhang, Z. Wang, M. Yu, In situ

761   fabrication of a novel S-scheme heterojunction photocatalyts $Bi_2O_3/P-C_3N_4$ to enhance

762   levofloxacin removal from water, Separation and Purification Technology. 268 (**2021**).

Click here to access/download
Supplementary Material
Supporting Information.docx

Declaration of interests

☒ The authors declare that they have no known competing financial interests or personal relationships that could have appeared to influence the work reported in this paper.

☐The authors declare the following financial interests/personal relationships which may be considered as potential competing interests: